

---

# Fréchet Wavelet Distance: A Domain-Agnostic Metric for Image Generation

---

**Lokesh Veeramacheneni**

High-Performance Computing and Analytics Lab  
University of Bonn  
Bonn, 53115  
*lokiv@uni-bonn.de*

**Moritz Wolter**

High-Performance Computing and Analytics Lab  
University of Bonn  
Bonn, 53115  
*moritz.wolter@uni-bonn.de*

**Hildegard Kuehne**

Multimodal Learning Group  
University of Bonn  
Bonn, 53115  
*kuehne@cs.uni-bonn.de*

**Juergen Gall**

Computer Vision Group  
University of Bonn  
Bonn, 53115  
*gall@iai.uni-bonn.de*

## Abstract

Modern metrics for generative learning like Fréchet Inception Distance (FID) demonstrate impressive performance. However, they suffer from various shortcomings, like a bias towards specific generators and datasets. To address this problem, we propose the Fréchet Wavelet Distance (FWD) as a domain-agnostic metric based on Wavelet Packet Transform ( $\mathcal{W}_p$ ). FWD provides a sight across a broad spectrum of frequencies in images with a high resolution, along with preserving both spatial and textural aspects. Specifically, we use  $\mathcal{W}_p$  to project generated and dataset images to packet coefficient space. Further, we compute Fréchet distance with the resultant coefficients to evaluate the quality of a generator. This metric is general-purpose and dataset-domain agnostic, as it does not rely on any pre-trained network while being more interpretable because of frequency band transparency. We conclude with an extensive evaluation of a wide variety of generators across various datasets that the proposed FWD is able to generalize and improve robustness to domain shift and various corruptions compared to other metrics.

## 1 Introduction

With the surge of generative neural networks, especially in the image domain, it becomes important to assess their performance in a robust and reliable way [14, 4, 43, 27]. FID [14] has emerged as the de facto standard for comparing generative image synthesis approaches, as FID scores align well with human perception [26] when comparing different runs of the same architecture. However, it also shows various shortcomings, such as its reliance on a pre-trained classification backbone, i.e., InceptionV3 trained on ImageNet. This, by design, introduces a class dependency into FID-scores leading to accidental distortions [45] and improved scores if the evaluation set resembles ImageNet or if the use of ImageNet weights in the generator pushes the output distribution towards ImageNet [26].

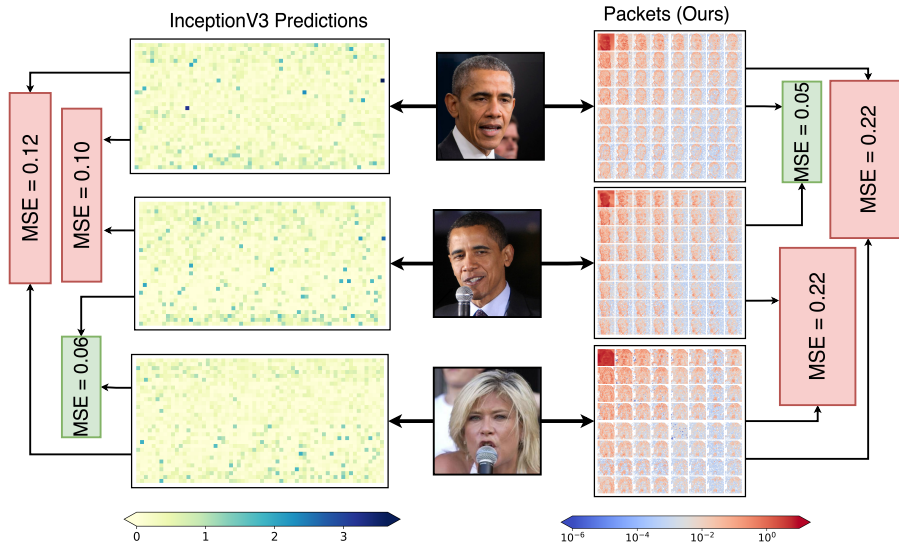


Figure 1: The first two images depict the same person, while the last image depicts a different person. Intuitively, the first two images are more similar than the other pairs of images. When computing the mean squared error between the images using the penultimate InceptionV3 activations or wavelet packets, we observe that the wavelet packets produce a low distance for the first two images, as expected. Surprisingly, according to InceptionV3, the last two images are similar since both images are classified as ‘microphone’ whereas the first image is classified as ‘groom’. All images are taken from [2].

To address the domain bias problem caused by the use of a pre-trained network, we propose an alternative metric based on the Wavelet Packet Transform ( $\mathcal{W}_p$ ). In contrast to other pure frequency [34] or spatial [55, 17] metrics, wavelets have the advantage that they combine both frequency and spatial aspects in one metric. While frequency information is important [9, 10, 40, 46, 60] it alone is insufficient to assess the quality of synthesized images without considering additional spatial information. Wavelets are thus an ideal representation for a metric comparing generative approaches for image synthesis. As FID, we utilize the Fréchet distance between the real and generated set of images as a distance measure, but it is not computed based on InceptionV3 activation maps. Instead, it utilizes the wavelet-packet frequency band representations of  $\mathcal{W}_p$  as illustrated in Figs. 1 and 3. To this end, we first use  $\mathcal{W}_p$  to transform every image, where we use the wavelet transform at a fixed level. We then compute the Fréchet distance for each packet of the transform and average them over all packets. The proposed Fréchet Wavelet Distance (FWD) thus considers the spatial information as well as all frequency bands.

To quantitatively assess those characteristics, we evaluate the proposed metric in terms of its domain bias and robustness. We further compare the proposed FWD to domain-agnostic methods like the Structural Similarity Index Measure (SSIM) and the Peak Signal to Noise Ratio (PSNR) as well as domain-dependent metrics like FID and Kernel Inception Distance (KID) on five standard datasets. We show that FWD is a more robust metric that does not suffer from the domain bias and can thus be applied to any dataset. We also show that some odd FID results can be attributed to the dataset bias.

In summary, this paper makes the following contributions: (1) We propose the Fréchet Wavelet Distance (FWD) as a dataset- and domain-agnostic metric for evaluating generative approaches for image synthesis. (2) FWD is an interpretable metric, as the wavelet packet transform splits the frequency space into hierarchically organized, discrete subbands. (3) We show in an extensive evaluation that the proposed method is robust to corruption, perturbation, and distractors.

## 2 Related Work

### 2.1 Metrics for generative learning

We consider domain-agnostic and domain-dependent metrics. Traditional image distance metrics are a possible domain-agnostic option to evaluate the quality of generated images. The Structural Similarity Index Measure (SSIM), for example, is a longstanding pairwise image distance metric [56]. The score takes luminance, contrast, and structure into account. Along with SSIM, Peak Signal to Noise Ratio (PSNR) is the most used metric for Image quality assessment. PSNR is computed as a logarithmic ratio between the maximum pixel value of the original image and the root mean square error between the original image and its noisy approximation [17]. Previous work reports SSIM’s preference for blurry images [42], which disagrees with human perception.

Having discussed domain-agnostic methods, we now turn to domain-dependent approaches. A generative model should generate novel image samples that mirror the training set sample distribution, including data diversity. In a vision context, [43] proposed the Inception Score (IS) as a measure of image quality, independent of the target dataset statistics. The IS is computed by measuring the entropy of the class probabilities of an InceptionV3. The score builds upon the assumption, that a generative network that has converged to a meaningful solution will produce images that will allow InceptionV3 to make predictions with certainty. A certain InceptionV3 has a low prediction entropy. IS has been found to be sensitive to different Imagenet training runs [3]. Furthermore, it does not use the statistics of the real data distribution a Generative Adversarial neural Network (GAN) is trained to model [14]. In response [14] proposes FID. Instead of measuring the entropy at the final layer FID is computed by evaluating the Fréchet distance [8] the penultimate network activations computed on both the true and synthetic images. Today, comparing high-level inception net features using an FID-score [14] enjoys widespread adoption. Variants exist, Kernel Inception Distance (KID) [4], for example, relaxes the multi-variate Gaussian assumption of FID and measures the polynomial kernel distance between Inception features of generated and training dataset. [4] kept the InceptionV3 backbone and replaced Fréchet distance with kernel distance. While FID captures general trends well, the literature also discusses its drawbacks. [26] empirically studies the effect of ImageNet classes on FID for non-ImageNet datasets by using GradCAM. Furthermore [26] examines ImageNet bias using Projected Fast GAN (Proj. FastGAN) and StyleGAN2. Compared to StyleGAN2, Proj. FastGAN produces more accidental distortions. Surprisingly, Proj. FastGAN’s FID is comparable to StyleGAN2’s in their experiment. [5] found a generator-dependent architecture bias, which limits our ability to compare samples for smaller datasets with 50K or fewer images. Additionally, [36] found that both FID and KID are highly sensitive to resizing and compression. [3] reported FID sensitivity with respect to different ImageNet training runs. While comparing Tensorflow and Pytorch implementations, [36] measured inconsistent scores due to differing resizing implementations. Finally, FID scores are hard to reproduce unless all details regarding its computation are carefully disclosed [1]. This motivates the search for additional quality metrics.

### 2.2 Spectral Methods

Prior work found neural networks are spectrally biased [40]. Many architectures favor low-frequency content [9, 11, 60, 65]. Related articles rely on the Fourier or Wavelet transform to understand frequency bias. Wavelet transforms as pioneered by [32] and [6] have a solid track record in signal processing. The Fast Wavelet Transform (FWT) and the closely related Wavelet Packet Transform ( $\mathcal{W}_p$ ), are starting to appear more frequently in the deep learning literature. Applications include Convolutional Neural Network (CNN) augmentation [58], style transfer [63], image denoising [30, 44], image coloring [29], face aging [31], video enhancement [54], face super-resolution [18], and generative machine learning [11, 12, 65, 39]. [13] uses the Fourier transform to measure the quality of human motion forecasting. [65] uses a FWT to remove artifacts from generated images. [39] focuses on the wavelet transform to increase the inference speed of diffusion models. This work proposes to use the Wavelet Packet Transform ( $\mathcal{W}_p$ ) as an interpretable metric for image generators.

## 3 Fréchet Wavelet Distance (FWD)

We want to tackle the problem of dataset-domain bias. To this end, we propose FWD, which in turn leverages the Wavelet Packet Transform ( $\mathcal{W}_p$ ). We require two-dimensional filters for image

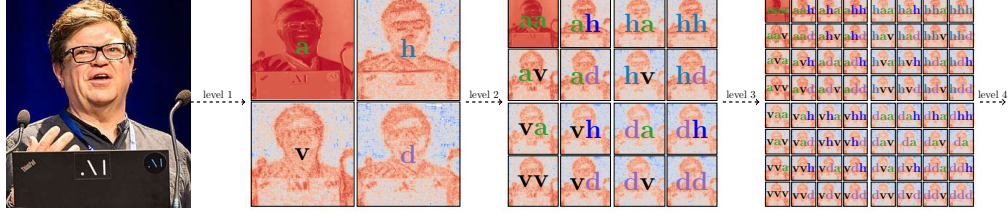


Figure 2: Illustration of the Wavelet Packet Transform ( $\mathcal{W}_p$ ). For visualization purposes, we depict level-3 transform. Even though all experiments later used level-4 transform. Image from [57].

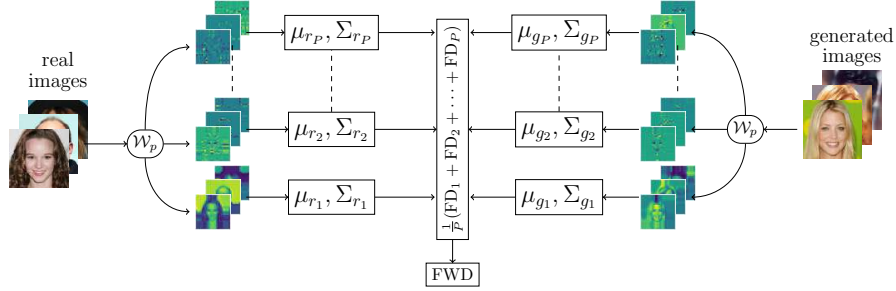


Figure 3: Fréchet Wavelet Distance (FWD) computation flow-chart.  $\mathcal{W}_p$  denotes the wavelet-packet transform. Not all packet coefficients are shown, dashed lines indicate omissions. We compute individual Fréchet Distances for each frequency band.

processing where we use Haar wavelets. Consequently, we construct filter quadruples from the original single-dimensional filter pairs. The process uses outer products [53]:

$$\mathbf{h}_a = \mathbf{h}_L \mathbf{h}_L^T, \mathbf{h}_h = \mathbf{h}_L \mathbf{h}_H^T, \mathbf{h}_v = \mathbf{h}_H \mathbf{h}_L^T, \mathbf{h}_d = \mathbf{h}_H \mathbf{h}_H^T \quad (1)$$

With  $a$  for the approximation filter,  $h$  for the horizontal filter,  $v$  for the vertical filter, and  $d$  for the diagonal filter [28]. We construct a  $\mathcal{W}_p$ -tree for images with these two-dimensional filters as illustrated in Fig. 2. Recursive convolution operations with the filter quadruples, i.e.,

$$\mathbf{C}_{\mathcal{F}_l} * \mathbf{h}_j = \mathbf{C}_{\mathcal{F}_{l+1}} \quad (2)$$

at every recursion step where  $*$  denotes a two-dimensional convolution with a stride of two. The filter codes  $\mathcal{F}_{l+1}$  are constructed by applying all  $j \in [a, h, v, d]$  filters to the previous filter codes  $\mathcal{F}_l$ . Initially, the set of inputs  $F_l$  will only contain the original image  $\mathbf{C}_{F_0} = \{X\}$  as shown in Fig. 2. At level one, we obtain the result of all four convolutions with the input image and have  $F_1 = [a, h, v, d]$ . At level two, we repeat the process for all elements in  $F_1$ .  $F_2$  now contains two-character keys  $[aa, ah, av, ad, \dots, dv, dd]$  as illustrated in Fig. 2. We typically continue this process until level 4 in this paper. We arrange the coefficients in  $\mathbf{C}_{\mathcal{F}_l}$  as tensors  $\mathbf{C}_l \in \mathbb{R}^{P, H_p, W_p}$  for the final layer. The total number of packages at every level is given by  $P = 4^l$ , and  $H_p = \frac{H}{4^l}$  and  $W_p = \frac{W}{4^l}$  where we denote the image height and width as  $H$  and  $W$ . We provide more details on  $\mathcal{W}_p$  in the Supplementary.

Figure 3 illustrates how we compute the FWD. The process relies on the wavelet packet transform, as previously discussed. We process  $N$  images with  $C$  channels in parallel  $\mathcal{W}_p : I_s \in \mathbb{R}^{N \times H \times W \times C} \rightarrow \mathbf{C} \in \mathbb{R}^{N \times P \times H_p \times W_p \times C}$ .  $H, W$  denotes image height and width as before. To facilitate the ensuing metric evaluation, we flatten the last axes into  $(H_p \cdot W_p \cdot C)$ . Before computing the packets, all pixels are divided by 255 to re-scale all values to  $[0,1]$ . The metric is computed in three steps. First, we compute the individual packet mean via

$$\mu_p(I_N) = \frac{1}{N} \sum_{n=1}^N \mathcal{W}(I_n)_p, \quad (3)$$

where  $I_n$  is the  $n^{th}$  image in the dataset and  $p$  represent the corresponding packet from  $P$  packets. Then we compute the covariance matrix as

$$\Sigma_p(I_N) = \frac{1}{N-1} \sum_{n=1}^N (\mathcal{W}(I_n)_p - \mu_p(I_N)) (\mathcal{W}(I_n)_p - \mu_p(I_N))^T \quad (4)$$

Here  $\mu \in \mathbb{R}^{P \times C \cdot H_p \cdot W_p}$  estimate the mean across the number of images, and  $\Sigma \in \mathbb{R}^{P \times C \cdot H_p \cdot W_p \times C \cdot H_p \cdot W_p}$  represents the covariance among all the coefficients. Now we are ready to compute the distances given the packet mean and covariance values,

$$FD_p(r, g) = d(\mathcal{N}(\mu_{r_p}, \Sigma_{r_p}), \mathcal{N}(\mu_{g_p}, \Sigma_{g_p}))^2 = \|\mu_{r_p} - \mu_{g_p}\|_2^2 + \text{tr}[\Sigma_{r_p} + \Sigma_{g_p} - 2\sqrt{\Sigma_{r_p}\Sigma_{g_p}}]. \quad (5)$$

With  $r$  and  $g$  denoting the real and generated images.  $\text{tr}$  denotes the trace operation. Utilising the above computed per-packet statistics for both real  $(\mu_r, \Sigma_g)$  and generated samples  $(\mu_r, \Sigma_g)$ , we measure the mean of Fréchet Distance (Equation 5) across all packets

$$\text{FWD} = \frac{1}{P} \sum_{p=1}^P d(\mathcal{N}(\mu_{r_p}, \Sigma_{r_p}), \mathcal{N}(\mu_{g_p}, \Sigma_{g_p}))^2. \quad (6)$$

By averaging the distances of all frequency bands, the FWD captures frequency information across the spectrum.

## 4 Experiments

Our first series of experiments reevaluates FID, KID, PSNR, SSIM and FWD on six standard datasets. All our experiments rely on the same code base.

**Implementation** We use PyTorch [37] for neural network training and evaluation and compute FID using [47] as recommended by [15]. We work with the wavelet filter coefficients provided by PyWavelets [28]. We chose the PyTorch-Wavelet-Toolbox [59] software package for GPU support. Furthermore, we employ scikit-image [52] to compute SSIM and PSNR scores. KID is computed using the code from [4].

### 4.1 Comparison to State-of-the-art

To understand the spectral qualities of existing generative methods for image synthesis, we evaluated various diffusion and GAN models across a wide range of benchmarks.

**Datasets** We compare common metrics and our FWD on CIFAR-10 [25], Large-scale Celeb Faces Attributes High Quality (CelebA-HQ) [20], the Church and Bedroom subsets of the Large-scale Scene UNderstanding (LSUN) dataset [64], and finally ImageNet [41]. In order to retain consistent spatial and frequency characteristics across various image sizes, we use level 4 packet transform for 256x256 images. Furthermore, we reduce the transformation level by factor of 1 for reduction in image size by half.

**Generators** For the evaluation, we use the diffusion approaches Denoising Diffusion Probabilistic Models (DDPM) [16], Denoising Diffusion Implicit Models (DDIM) [49], Improved Diffusion [35], Diffusion Transformer [38], as well as the GAN approaches DDGAN [61], StyleGAN2 [22], StyleSwin [65]. We used the publicly available code for all approaches and compared the unconditionally generated images to the original dataset.

**Hyperparameters** No optimization is done in this section. All generators run with weights as provided by the respective paper authors.

**Metrics** We compute FID, KID, PSNR, SSIM [56] and finally our own FWD. Table 1 lists all numbers. FID-scores are from the standard implementation by [47].

For CIFAR10, we use 50K images to evaluate both metrics. The ImageNet numbers are computed with 50K images from the validation set. For CelebAHQ and LSUN we work with 30K images.

Considering CelebA-HQ, FID, KID, and FWD agree most of the time. Only, DDPM and StyleSwin are swapped. FWD therefore delivers a comparable quality signal in this case. The ordering remains largely unchanged for LSUN churches. In terms of FWD, we observe a stable ranking across the two datasets. Except DDPM and StyleSwin, which are swapped. Given the different nature of both datasets, we argue small changes like these are reasonable. We observe larger changes in magnitude for FID-scores when making the switch from CelebA-HQ to LSUN churches. The switch moves us towards ImageNet, since "church" is an ImageNet class, but "face" is not. Figure 10b depicts the histograms of top-15 classes classified by InceptionV3 for LSUN churches, DDPM and StyleSwin. We observe that StyleSwin matches the activation histograms of LSUN churches more accurately than the DDPM. This observation is a manifestation of domain bias and explains the FID inconsistency for both generators.

Table 1: Comparing recent generative models using Fréchet Wavelet Distance (FWD), Fréchet Inception Distance (FID), Structural Similarity Index Measure (SSIM), Kernel Inception Distance (KID), and Peak Signal to Noise Ratio (PSNR).

Dataset	Image Size	Method	FID↓	KID↓	PSNR↑	SSIM↑	FWD↓ (ours)
CelebAHQ	256	DDIM [49]	32.333	0.0313	9.467	0.255	12.317
		DDPM [16]	19.101	0.0152	<b>9.538</b>	<b>0.277</b>	4.697
		StyleSwin [65]	23.257	0.0264	9.105	0.275	1.528
		StyleGAN2 [23]	15.439	0.0155	8.906	0.253	0.476
		DDGAN [61]	<b>7.203</b>	<b>0.0034</b>	8.976	0.258	<b>0.408</b>
Churches	256	DDIM [49]	11.775	0.0043	8.701	0.007	4.919
		DDPM [16]	9.484	0.0036	8.548	0.001	3.546
		StyleSwin [65]	<b>3.187</b>	<b>0.0005</b>	<b>9.536</b>	0.005	2.835
		StyleGAN2 [23]	4.309	0.0007	8.804	<b>0.009</b>	<b>0.753</b>
Bedrooms	256	DDIM [49]	25.857	0.0094	<b>9.258</b>	0.007	9.521
		DDPM [16]	<b>16.251</b>	<b>0.0058</b>	8.791	<b>0.011</b>	<b>5.187</b>
CIFAR10	32	DDIM [49]	32.531	0.0239	8.461	0.011	14.803
		DDPM [16]	9.978	0.0075	8.975	0.013	2.506
		Imp. Diff. (VLB) [35]	15.067	0.3779	<b>9.053</b>	0.012	0.641
		StyleGAN2 [22]	17.313	0.0201	8.801	0.012	0.554
		Imp. Diff. (Hybrid) [35]	16.892	0.0395	8.873	<b>0.016</b>	0.303
		DDGAN [61]	<b>3.465</b>	<b>0.0008</b>	8.811	0.012	<b>0.211</b>
ImageNet	64	Imp. Diff. (VLB) [35]	42.257	0.1132	<b>8.829</b>	0.009	2.221
		BigGAN	5.327	0.0731	8.529	0.054	0.441
		Imp. Diff. (Hybrid) [35]	<b>3.947</b>	<b>0.0724</b>	8.472	<b>0.055</b>	<b>0.392</b>

We also consider the LSUN-Bedrooms and ImageNet 64 data sets, where FID and FWD agree. We expect pristine performance for FID on ImageNet since this setting is perfectly in its data-domain. Our FWD produces the same ranking on CIFAR-10 and CelebA-HQ, while FID is not consistent. We argue the inconsistency stems from a shift in the underlying data bias and does not truly reflect generator quality.

## 4.2 Effect of domain bias

We noticed in the previous section that metrics which rely on ImageNet features focus on ImageNet-related information. This behavior is desired when we score generators on ImageNet or similar datasets. When working with unrelated data sets, this behavior is misleading.

**Data-Sets** This section studies CelebA-HQ [20], Flickr Faces High Quality (FFHQ) and, DNDD-Dataset a dataset of Agricultural images [62]. These data sets contain images that are very different from those in the ImageNet-Set. More information about DNDD-Dataset can be found in the supplementary material.

**Generators** We study data-set domain bias effects using the Denoising Diffusion GAN (DDGAN), Proj. FastGAN and StyleGAN2 networks. Proj. FastGAN is particularly interesting. To improve training convergence its discriminator relies on ImageNet weights [45]. Prior work found this architecture to improve FID on image datasets far from ImageNet [26].

**Hyperparameters** To examine the effect of data-set bias, we require generators, which are tuned to produce output that resembles our datasets' distribution. We train the Proj. FastGAN for 100 epochs on CelebA-HQ and separately on the DNDD-Dataset. In both cases with a learning rate of  $2e-4$  and a batch size of 64 on 8 A100 GPUs. For FFHQ, weights are available. Pretrained weights are also available for DDGAN on CelebAHQ [61]. On the DNDD-Dataset, we train DDGAN for 150 epochs with a learning rate of  $1e-4$  and batch size of 8 on the same hardware. For StyleGAN2 we the pretrained weights with the code from [23].

Table 2 lists the FID, and FWD values for all datasets images from the aforementioned generators. Across all datasets, ImageNet FID prefers Proj. FastGAN images. Figure 4a and 4b depict images



(a) Proj. FastGAN on CelebA-HQ FID: 6.358 FWD: 1.388



(b) DDGAN on CelebA-HQ FID: 7.641 FWD: 0.408



(c) Proj. FastGAN on DNDD-Dataset FID: 4.675 FWD: 1.442



(d) DDGAN on DNDD-Dataset FID: 26.223 FWD: 1.357

Figure 4: Uncurated samples from (a) Proj. FastGAN, (b) DDGAN models on CelebA-HQ dataset. (c) and (d) represent samples from both the models on DNDD-Dataset respectively. The FID-ranking fluctuates, whereas our metric (FWD) provides a consistent ranking irrespective of the dataset.

Table 2: Comparison of biased and unbiased Fréchet distances. FID denotes the standard formulation using an InceptionV3 trained on ImageNet. To eliminate the imagenet bias we re-trained InceptionV3. The FID (CelebA) and FID (DNDD-Dataset) columns list the distances measured using the retrained networks as a backbone. We find that re-training is possible only for large datasets where sufficient data is available. FWD consistently provides a meaningful metric.

Dataset	Generator	FID (ImageNet) ↓	FID (CelebA) ↓	FID (DNDD-Dataset) ↓	FWD(ours) ↓
CelebA-HQ	Proj. FastGAN	<b>6.358</b>	5.602	1.824	1.388
	DDGAN	7.641	<b>3.145</b>	<b>0.558</b>	<b>0.408</b>
DNDD-Dataset	Proj. FastGAN	<b>4.675</b>	<b>0.861</b>	<b>20.937</b>	1.442
	DDGAN	26.233	2.325	52.521	<b>1.357</b>
FFHQ	Proj. FastGAN	<b>4.106</b>	2.204	3.549	0.651
	StyleGAN2	4.282	<b>0.897</b>	<b>0.393</b>	<b>0.312</b>

from the CelebA-HQ variants of Proj. FastGAN and DDGAN. Deformations are visible in the images from Proj. FastGAN on the left. Generally, we found more deformations in Proj. FastGAN images compared to DDGAN images. This confirms what we see in the random sample in Figures 4a and 4b. Consequently, ImageNet FID’s preference is surprising, as we would expect DDGAN to come out on top. FWD correctly places DDGAN ahead of Proj. FastGAN. Our results on FFHQ in the bottom row of Table 2 confirm this pattern.

Additional results on the DNDD-Dataset further corroborate this argument. Once more FID prefers Proj. FastGAN, this time with a significant margin. Figures 4c and 4d show both networks have converged and produce meaningful images. To confirm the bias on DNDD-Dataset, we perform histogram matching for the top-15 as recognized by InceptionV3 trained on ImageNet. The histograms appear in Figure 11. We observe that Proj. FastGAN pushes InceptionV3 to produce a more ImageNet-like activation distribution, which improves the score. However, in this case this distribution is irrelevant. Consequently, FID scores are unreliable. FWD in turn, produces scores which place DDGAN slightly ahead of Proj. FastGAN. A result consistent with earlier experiments.

Re-training InceptionV3 could be a solution. The network features will be relevant if we can find a classification problem close to the distribution of interest. We train InceptionV3 on Large-scale Celeb Faces Attributes (CelebA). CelebA comes with 40 facial attributes, which we use to train. Once converged we see an exact match ratio of 90%. We proceed by computing FID with the retrained backbone. The FID (CelebA) column of Table 2, lists the corresponding scores. The order inverts. FID (CelebA) and FWD now agree.

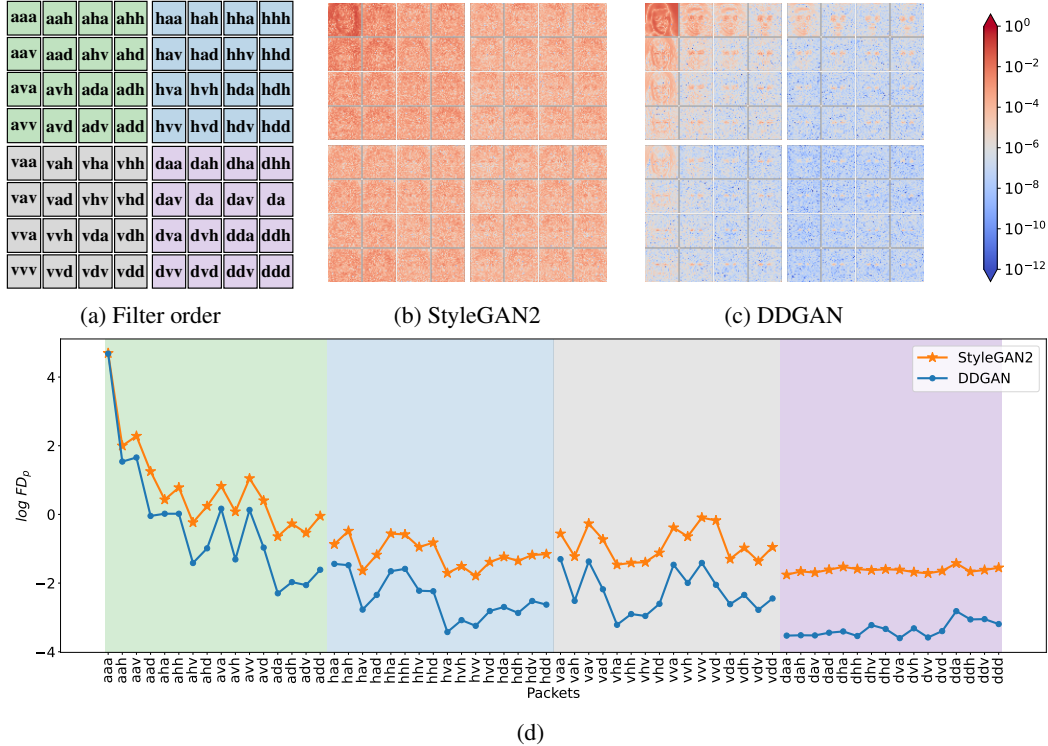


Figure 5: Interpretation of FWD. (a) represents the blueprint for level-3  $\mathcal{W}_p$  transformation. (b) and (c) depict the mean absolute packet difference between CelebA-HQ dataset and StyleGAN2, and DDGAN respectively. (d) shows the per-packet Fréchet distances for StyleGAN2 in orange and DDGAN in blue.

However, in the case of the agricultural data set, the retrained FID (CelebA) remains biased, while FWD produces meaningful domain agnostic results. DNDD-Dataset contains 3600 images with 7 classes. Networks are tasked with detecting nutrient deficiency in the soil, such as Sodium, Calcium, unfertilized, and 4 others. Once more, we use a re-trained InceptionV3 backbone for the FID computation. In comparison to CelebA or ImageNet, this is a small data set. The small size explains the problems. We trained until convergence, but the data set is too small. The re-trained network does to provide meaningful features. We believe this is a very interesting use case since it illustrates that the FWD is not just free from data bias, it also provides meaningful feedback for low resource tasks, where retraining InceptionV3 is not feasible.

### 4.3 FWD interpretability

A generative metric is interpretable if and only if we can understand the underlying mechanics that produce the ranking. This section explains the decisions made by FWD in one specific case.

**Dataset and Generators** We use CelebA-HQ and we focus on samples from DDGAN and StyleGAN2.

Section 3 formulates FWD as an average of per packet FWD scores. This design choice allows us to understand the overall FWD-score in terms of the individual packet coefficients for each frequency band. Figure 5b and 5c depict the mean absolute difference per packet between the original CelebA-HQ and generated samples from StyleGAN2 and DDGAN respectively. Figure 5d presents both generators' per-packet FWD. Figure 5(d) shows that DDGAN has a lower Fréchet distance per packet than StyleGAN2 across the entire spectrum. (b) and (c) confirm FWD because the mean packet difference is larger for StyleGAN2 (b) than DDGAN (c). Overall, we observe that the mean absolute packets translate into per packet Fréchet distance-scores, which validates the FWD overall.



Table 3: StyleGAN2-FFHQ matching fringe features with 250K images with mean and std for 5 runs.

Metric	Random Images	FID-Optimized Images	Change
FID	$4.278 \pm 0.019$	<b><math>2.031 \pm 0.005</math></b>	-47%
KID	$0.00118 \pm 0.00019$	<b><math>0.0003 \pm 0.00019</math></b>	-25%
FWD	<b><math>0.338 \pm 0.017</math></b>	$0.398 \pm 0.009$	+2.5%

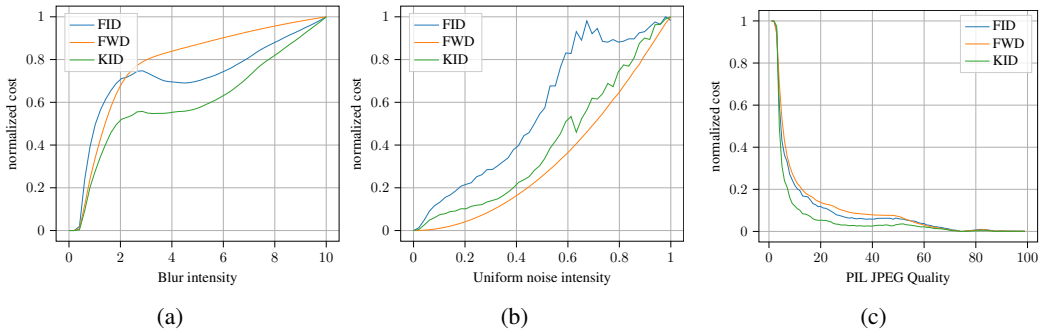


Figure 6: Figures depicting the effect of perturbations like (a) Gaussian blurs and (b) uniform noise corruption as well as (c) jpeg-compression on FID, FWD and KID.

#### 4.4 Evaluation of Robustness

The section follows up on prior work by Kynkäänniemi et al. [26]. The authors generate a large set of samples and find a specific combination of images with an optimal FID. Weighted sampling produces possible combinations. The process chooses images according to a corresponding weight. The weights or drawing probabilities are optimized with FID as the objective function. We follow this process and sample 50K images from a large set with optimized weights as probabilities. We employ generated images from StyleGAN2 and real-world images from the FFHQ dataset. Table 3 lists the resulting FID and FWD scores. We observe that FWD is robust to FID optimization. We speculate this may be the result of its independent vision space. It is of course possible to optimize our metric this way, but it will be tougher to optimize FID and FWD jointly as their feature representation space is different.

In addition to FID optimization, we study the impact of image perturbation in Figure 6. We find that FWD is closer to a bijective mapping in the presence of perturbation than FID. This behavior is desirable since we would always expect a larger distance if for example more noise is added. This is not always the case for FID. Consider for example the last quarter of the uniform noise intensity in (b), where FID falls even though more noise is added. SSIM responds in a very clean way to image perturbations in this case. But the metric is pairwise in nature, which limits its appeal in unconditional settings such as the one we are considering here.

### 5 Limitations and Impact

The FWD is a useful addition for tasks far from ImageNet or when a frequency-based metric is desired. For generative tasks on ImageNet, its utility will be limited since we expect FID or KID to perform well in this case. Furthermore, for datasets close to ImageNet FID captures semantic meaning, where FWD will instead rely more on frequency and spatial information. While FWD is robust to FID, optimization is presented by [26]. It is certainly also possible to optimize FID and FWD jointly. We expect this task to be harder since FWD must also appear in the cost function. This paper re-evaluates generative learning methods. We do not expect our evaluation to negatively impact society.

### 6 Conclusion

Modern generative models are biased in frequency[9], while modern metrics like FID and KID come with a domain bias [26]. Addressing both problems requires metrics that consider frequency infor-

mation without introducing a domain bias. Existing domain-agnostic metrics like SSIM and PSNR are pairwise metrics and, therefore, unsuitable in unconditional generation settings. Consequently, this paper proposed a robust, interpretable, and domain-agnostic metric built on the wavelet packet transform for comparing image synthesis approaches.

## 7 Acknowledgements

This research was funded by Bundesministerium für Bildung und Forschung (BMBF) via WestAI under grant no. “01IS22094E WEST-AI” and BNTrAInee project under “16DHBK1022”. We thank Gauss Centre for Supercomputing e.V. ([www.gauss-centre.eu](http://www.gauss-centre.eu)) for supporting this project by providing computing time through the John von Neumann Institute for Computing (NIC) on the GCS Supercomputer JUWELS at Jülich Supercomputing Centre (JSC). Finally, we would like to thank Dr. Bartosz Kostrzewa for helping with the experiments on JSC and Michael Kuckertz from the HPC team for providing last-minute resources.

## References

- [1] Evaluating diffusion models. <https://huggingface.co/docs/diffusers/conceptual/evaluation>, 2024. Accessed: 2024-04-11.
- [2] Flickr image data base. <https://www.flickr.com>, 2024. Accessed: 2024-09-30, Images are distributed using various Creative Commons Licenses.
- [3] Shane T. Barratt and Rishi Sharma. A note on the inception score. *ICML 2018 workshop on Theoretical Foundations and Applications of Deep Generative Models.*, 2018.
- [4] Mikolaj Binkowski, Danica J. Sutherland, Michael Arbel, and Arthur Gretton. Demystifying MMD gans. In *6th International Conference on Learning Representations, ICLR 2018, Vancouver, BC, Canada, April 30 - May 3, 2018, Conference Track Proceedings*, 2018.
- [5] Min Jin Chong and David A. Forsyth. Effectively unbiased FID and inception score and where to find them. In *2020 IEEE/CVF Conference on Computer Vision and Pattern Recognition, CVPR 2020, Seattle, WA, USA, June 13-19, 2020*, pages 6069–6078. Computer Vision Foundation / IEEE, 2020.
- [6] Ingrid Daubechies. *Ten Lectures on Wavelets*. Society for Industrial and Applied Mathematics, 1992.
- [7] Prafulla Dhariwal and Alexander Nichol. Diffusion models beat gans on image synthesis. *Advances in neural information processing systems*, 34:8780–8794, 2021.
- [8] DC Dowson and BV666017 Landau. The fréchet distance between multivariate normal distributions. *Journal of multivariate analysis*, 12(3):450–455, 1982.
- [9] Ricard Durall, Margret Keuper, and Janis Keuper. Watch your up-convolution: Cnn based generative deep neural networks are failing to reproduce spectral distributions. In *Proceedings of the IEEE/CVF conference on computer vision and pattern recognition*, pages 7890–7899, 2020.
- [10] Tarik Dzanic, Karan Shah, and Freddie Witherden. Fourier spectrum discrepancies in deep network generated images. *Advances in neural information processing systems*, 33:3022–3032, 2020.
- [11] Rinon Gal, Dana Cohen Hochberg, Amit Bermano, and Daniel Cohen-Or. Swagan: A style-based wavelet-driven generative model. *ACM Trans. Graph.*, 40(4), July 2021.
- [12] Florentin Guth, Simon Coste, Valentin De Bortoli, and Stephane Mallat. Wavelet score-based generative modeling. *Advances in Neural Information Processing Systems*, 35:478–491, 2022.
- [13] Alejandro Hernandez, Jurgen Gall, and Francesc Moreno-Noguer. Human motion prediction via spatio-temporal inpainting. In *Proceedings of the IEEE/CVF International Conference on Computer Vision*, pages 7134–7143, 2019.

- [14] Martin Heusel, Hubert Ramsauer, Thomas Unterthiner, Bernhard Nessler, and Sepp Hochreiter. Gans trained by a two time-scale update rule converge to a local nash equilibrium. *Advances in neural information processing systems*, 30, 2017.
- [15] Martin Heusel, Thomas Unterthiner, Wendy Kan, Mark Hamilton, Zejian Li, Marc Uecker, Wang Penghui, and Partik Joshi. Two time-scale update rule for training gans. <https://github.com/bioinf-jku/TTUR>, 2017.
- [16] Jonathan Ho, Ajay Jain, and Pieter Abbeel. Denoising diffusion probabilistic models. In Hugo Larochelle, Marc’Aurelio Ranzato, Raia Hadsell, Maria-Florina Balcan, and Hsuan-Tien Lin, editors, *Advances in Neural Information Processing Systems 33: Annual Conference on Neural Information Processing Systems 2020, NeurIPS 2020, December 6-12, 2020, virtual*, 2020.
- [17] Alain Horé and Djemel Ziou. Image quality metrics: PSNR vs. SSIM. In *20th International Conference on Pattern Recognition, ICPR 2010, Istanbul, Turkey, 23-26 August 2010*, pages 2366–2369. IEEE Computer Society, 2010.
- [18] Huaibo Huang, Ran He, Zhenan Sun, and Tieniu Tan. Wavelet-srnet: A wavelet-based cnn for multi-scale face super resolution. In *Proceedings of the IEEE international conference on computer vision*, pages 1689–1697, 2017.
- [19] Arne Jensen and Anders la Cour-Harbo. *Ripples in mathematics: the discrete wavelet transform*. Springer Science & Business Media, 2001.
- [20] Tero Karras, Timo Aila, Samuli Laine, and Jaakko Lehtinen. Progressive growing of gans for improved quality, stability, and variation. In *6th International Conference on Learning Representations, ICLR 2018, Vancouver, BC, Canada, April 30 - May 3, 2018, Conference Track Proceedings*, 2018.
- [21] Tero Karras, Miika Aittala, Samuli Laine, Erik Härkönen, Janne Hellsten, Jaakko Lehtinen, and Timo Aila. Alias-free generative adversarial networks. *Advances in Neural Information Processing Systems*, 34:852–863, 2021.
- [22] Tero Karras, Samuli Laine, and Timo Aila. A style-based generator architecture for generative adversarial networks. In *Proceedings of the IEEE/CVF conference on computer vision and pattern recognition*, pages 4401–4410, 2019.
- [23] Tero Karras, Samuli Laine, Miika Aittala, Janne Hellsten, Jaakko Lehtinen, and Timo Aila. Analyzing and improving the image quality of stylegan. In *Proceedings of the IEEE/CVF conference on computer vision and pattern recognition*, pages 8110–8119, 2020.
- [24] Diederik P. Kingma and Max Welling. Auto-encoding variational bayes. In Yoshua Bengio and Yann LeCun, editors, *2nd International Conference on Learning Representations, ICLR 2014, Banff, AB, Canada, April 14-16, 2014, Conference Track Proceedings*, 2014.
- [25] Alex Krizhevsky, Geoffrey Hinton, et al. Learning multiple layers of features from tiny images. 2009.
- [26] Tuomas Kynkäänniemi, Tero Karras, Miika Aittala, Timo Aila, and Jaakko Lehtinen. The role of imagenet classes in fréchet inception distance. In *The Eleventh International Conference on Learning Representations, ICLR 2023, Kigali, Rwanda, May 1-5, 2023*. OpenReview.net, 2023.
- [27] Tuomas Kynkäänniemi, Tero Karras, Samuli Laine, Jaakko Lehtinen, and Timo Aila. Improved precision and recall metric for assessing generative models. In Hanna M. Wallach, Hugo Larochelle, Alina Beygelzimer, Florence d’Alché-Buc, Emily B. Fox, and Roman Garnett, editors, *Advances in Neural Information Processing Systems 32: Annual Conference on Neural Information Processing Systems 2019, NeurIPS 2019, December 8-14, 2019, Vancouver, BC, Canada*, pages 3929–3938, 2019.
- [28] Gregory Lee, Ralf Gommers, Filip Waselewski, Kai Wohlfahrt, and Aaron O’Leary. Pywavelets: A python package for wavelet analysis. *Journal of Open Source Software*, 4(36):1237, 2019.
- [29] Jin Li, Wanyun Li, Zichen Xu, Yuhao Wang, and Qiegen Liu. Wavelet transform-assisted adaptive generative modeling for colorization. *IEEE Transactions on Multimedia*, 2022.

- [30] Lin Liu, Jianzhuang Liu, Shanxin Yuan, Gregory Slabaugh, Aleš Leonardis, Wengang Zhou, and Qi Tian. Wavelet-based dual-branch network for image demoiréing. In *Computer Vision—ECCV 2020: 16th European Conference, Glasgow, UK, August 23–28, 2020, Proceedings, Part XIII 16*, pages 86–102. Springer, 2020.
- [31] Yunfan Liu, Qi Li, and Zhenan Sun. Attribute-aware face aging with wavelet-based generative adversarial networks. In *Proceedings of the IEEE/CVF Conference on Computer Vision and Pattern Recognition*, pages 11877–11886, 2019.
- [32] Stéphane Mallat. A theory for multiresolution signal decomposition: The wavelet representation. *IEEE Trans. Pattern Anal. Mach. Intell.*, 11(7):674–693, 1989.
- [33] Stéphane Mallat. *A wavelet tour of signal processing*. Elsevier, 1999.
- [34] Manish Narwaria, Weisi Lin, Ian Vince McLoughlin, Sabu Emmanuel, and Liang-Tien Chia. Fourier transform-based scalable image quality measure. *IEEE Trans. Image Process.*, 21(8):3364–3377, 2012.
- [35] Alexander Quinn Nichol and Prafulla Dhariwal. Improved denoising diffusion probabilistic models. In *Proceedings of the 38th International Conference on Machine Learning*, volume 139 of *Proceedings of Machine Learning Research*, pages 8162–8171. PMLR, 18–24 Jul 2021.
- [36] Gaurav Parmar, Richard Zhang, and Jun-Yan Zhu. On aliased resizing and surprising subtleties in gan evaluation. In *Proceedings of the IEEE/CVF Conference on Computer Vision and Pattern Recognition*, pages 11410–11420, 2022.
- [37] Adam Paszke, Sam Gross, Soumith Chintala, Gregory Chanan, Edward Yang, Zachary DeVito, Zeming Lin, Alban Desmaison, Luca Antiga, and Adam Lerer. Automatic differentiation in pytorch. In *31st Conference on Neural Information Processing Systems (NIPS 2017)*, 2017.
- [38] William Peebles and Saining Xie. Scalable diffusion models with transformers. In *Proceedings of the IEEE/CVF International Conference on Computer Vision*, pages 4195–4205, 2023.
- [39] Hao Phung, Quan Dao, and Anh Tran. Wavelet diffusion models are fast and scalable image generators. In *IEEE/CVF Conference on Computer Vision and Pattern Recognition, CVPR 2023, Vancouver, BC, Canada, June 17-24, 2023*, pages 10199–10208. IEEE, 2023.
- [40] Nasim Rahaman, Aristide Baratin, Devansh Arpit, Felix Draxler, Min Lin, Fred Hamprecht, Yoshua Bengio, and Aaron Courville. On the spectral bias of neural networks. In *International Conference on Machine Learning*, pages 5301–5310. PMLR, 2019.
- [41] Olga Russakovsky, Jia Deng, Hao Su, Jonathan Krause, Sanjeev Satheesh, Sean Ma, Zhiheng Huang, Andrej Karpathy, Aditya Khosla, Michael Bernstein, Alexander C. Berg, and Li Fei-Fei. ImageNet Large Scale Visual Recognition Challenge. *International Journal of Computer Vision (IJCV)*, 115(3):211–252, 2015.
- [42] Chitwan Saharia, William Chan, Huiwen Chang, Chris Lee, Jonathan Ho, Tim Salimans, David Fleet, and Mohammad Norouzi. Palette: Image-to-image diffusion models. In *ACM SIGGRAPH 2022 Conference Proceedings*, pages 1–10, 2022.
- [43] Tim Salimans, Ian Goodfellow, Wojciech Zaremba, Vicki Cheung, Alec Radford, and Xi Chen. Improved techniques for training gans. *Advances in neural information processing systems*, 29, 2016.
- [44] Vishwanath Saragadam, Daniel LeJeune, Jasper Tan, Guha Balakrishnan, Ashok Veeraraghavan, and Richard G Baraniuk. Wire: Wavelet implicit neural representations. In *Proceedings of the IEEE/CVF Conference on Computer Vision and Pattern Recognition*, pages 18507–18516, 2023.
- [45] Axel Sauer, Kashyap Chitta, Jens Müller, and Andreas Geiger. Projected gans converge faster. In *Advances in Neural Information Processing Systems (NeurIPS)*, 2021.
- [46] Katja Schwarz, Yiyi Liao, and Andreas Geiger. On the frequency bias of generative models. *Advances in Neural Information Processing Systems*, 34:18126–18136, 2021.

- [47] Maximilian Seitzer. pytorch-fid: FID Score for PyTorch. <https://github.com/mseitzer/pytorch-fid>, August 2020. Version 0.3.0.
- [48] Jascha Sohl-Dickstein, Eric Weiss, Niru Maheswaranathan, and Surya Ganguli. Deep unsupervised learning using nonequilibrium thermodynamics. In *International conference on machine learning*, pages 2256–2265. PMLR, 2015.
- [49] Jiaming Song, Chenlin Meng, and Stefano Ermon. Denoising diffusion implicit models. In *9th International Conference on Learning Representations, ICLR 2021, Virtual Event, Austria, May 3-7, 2021*, 2021.
- [50] Gilbert Strang and Truong Nguyen. *Wavelets and filter banks*. SIAM, 1996.
- [51] Aaron Van Den Oord, Oriol Vinyals, et al. Neural discrete representation learning. *Advances in neural information processing systems*, 30, 2017.
- [52] Stéfan van der Walt, Johannes L. Schönberger, Juan Nunez-Iglesias, François Boulogne, Joshua D. Warner, Neil Yager, Emmanuelle Gouillart, Tony Yu, and the scikit-image contributors. scikit-image: image processing in Python. *PeerJ*, 2:e453, 6 2014.
- [53] Aparna Vyas, Soohwan Yu, and Joonki Paik. *Multiscale transforms with application to image processing*. Springer, 2018.
- [54] Jianyi Wang, Xin Deng, Mai Xu, Congyong Chen, and Yuhang Song. Multi-level wavelet-based generative adversarial network for perceptual quality enhancement of compressed video. In *European Conference on Computer Vision*, pages 405–421. Springer, 2020.
- [55] Zhou Wang, Alan C. Bovik, Hamid R. Sheikh, and Eero P. Simoncelli. Image quality assessment: from error visibility to structural similarity. *IEEE Trans. Image Process.*, 13(4):600–612, 2004.
- [56] Zhou Wang, Alan C Bovik, Hamid R Sheikh, and Eero P Simoncelli. Image quality assessment: from error visibility to structural similarity. *IEEE transactions on image processing*, 13(4):600–612, 2004.
- [57] Wiki. MS Windows NT kernel description. [https://en.wikipedia.org/wiki/Yann\\_LeCun#/media/File:Yann\\_LeCun\\_-\\_2018\\_\(cropped\).jpg](https://en.wikipedia.org/wiki/Yann_LeCun#/media/File:Yann_LeCun_-_2018_(cropped).jpg), 2024. Accessed: 2024-05-22.
- [58] Travis Williams and Robert Li. Wavelet pooling for convolutional neural networks. In *International conference on learning representations*, 2018.
- [59] Moritz Wolter, Felix Blanke, Jochen Garcke, and Charles Tapley Hoyt. ptwt - the pytorch wavelet toolbox. *Journal of Machine Learning Research*, 25(80):1–7, 2024.
- [60] Moritz Wolter, Felix Blanke, Raoul Heese, and Jochen Garcke. Wavelet-packets for deepfake image analysis and detection. *Machine Learning*, 111(11):4295–4327, 2022.
- [61] Zhisheng Xiao, Karsten Kreis, and Arash Vahdat. Tackling the generative learning trilemma with denoising diffusion gans. In *International Conference on Learning Representations*, 2022.
- [62] Jinhui Yi, Lukas Krusenbaum, Paula Unger, Hubert Hüging, Sabine J Seidel, Gabriel Schaaf, and Juergen Gall. Deep learning for non-invasive diagnosis of nutrient deficiencies in sugar beet using rgb images. *Sensors*, 20:5893, 2020.
- [63] Jaejun Yoo, Youngjung Uh, Sanghyuk Chun, Byeongkyu Kang, and Jung-Woo Ha. Photorealistic style transfer via wavelet transforms. In *Proceedings of the IEEE/CVF International Conference on Computer Vision*, pages 9036–9045, 2019.
- [64] Fisher Yu, Yinda Zhang, Shuran Song, Ari Seff, and Jianxiong Xiao. Lsun: Construction of a large-scale image dataset using deep learning with humans in the loop. *ArXiv*, abs/1506.03365, 2015.
- [65] Bowen Zhang, Shuyang Gu, Bo Zhang, Jianmin Bao, Dong Chen, Fang Wen, Yong Wang, and Baining Guo. Styleswin: Transformer-based gan for high-resolution image generation. In *Proceedings of the IEEE/CVF conference on computer vision and pattern recognition*, pages 11304–11314, 2022.

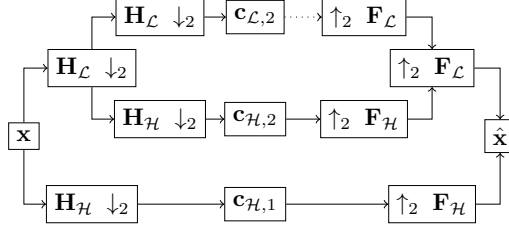


Figure 7: Overview of the Fast Wavelet Transform (FWT) computation.  $\mathbf{h}_{\mathcal{L}}$  denotes the analysis low-pass filter and  $\mathbf{h}_{\mathcal{H}}$  the analysis high pass filter.  $\mathbf{f}_{\mathcal{L}}$  and  $\mathbf{f}_{\mathcal{H}}$  the synthesis filter pair.  $\downarrow_2$  denotes downsampling with a factor of two,  $\uparrow_2$  means upsampling. The analysis transform on the left works with stride two convolutions. The synthesis or inverse transform on the right works with stride two transposed convolutions.  $\mathbf{H}_k$  and  $\mathbf{F}_k$  with  $k \in [\mathcal{L}, \mathcal{H}]$  denote the corresponding convolution operators.

## A Supplementary material

### A.1 Acronyms

$\mathcal{W}_p$  Wavelet Packet Transform

**CelebA** Large-scale Celeb Faces Attributes

**CelebA-HQ** Large-scale Celeb Faces Attributes High Quality

**CIFAR-10** Canadian Institute For Advanced Research-10

**CNN** Convolutional Neural Network

**DDGAN** Denoising Diffusion GAN

**DDIM** Denoising Diffusion Implicit Models

**DDPM** Denoising Diffusion Probabilistic Models

**DNDD-Dataset** Deep Nutrient Deficiency Dikopshof Dataset

**FFHQ** Flickr Faces High Quality

**FID** Fréchet Inception Distance

**FWD** Fréchet Wavelet Distance

**FWT** Fast Wavelet Transform

**GAN** Generative Adversarial neural Network

**IS** Inception Score

**KID** Kernel Inception Distance

**LSUN** Large-scale Scene UNderstanding

**MSE** Mean Squared Error

**Proj. FastGAN** Projected Fast GAN

**PSNR** Peak Signal to Noise Ratio

**SSIM** Structural Similarity Index Measure

**VAE** Variational AutoEncoder

### A.2 The fast wavelet and wavelet packet transforms

This supplementary section summarizes key wavelet facts as a convenience for the reader. See, for example, [50, 33] or [19] for excellent detailed introductions to the topic.

The Fast Wavelet Transform (FWT) relies on convolution operations with filter pairs. Figure 7 illustrates the process. The forward or analysis transform works with a low-pass  $\mathbf{h}_{\mathcal{L}}$  and a high-pass filter  $\mathbf{h}_{\mathcal{H}}$ . The analysis transform repeatedly convolves with both filters,

$$\mathbf{x}_s * \mathbf{1} \mathbf{h}_k = \mathbf{c}_{k,s+1} \quad (7)$$

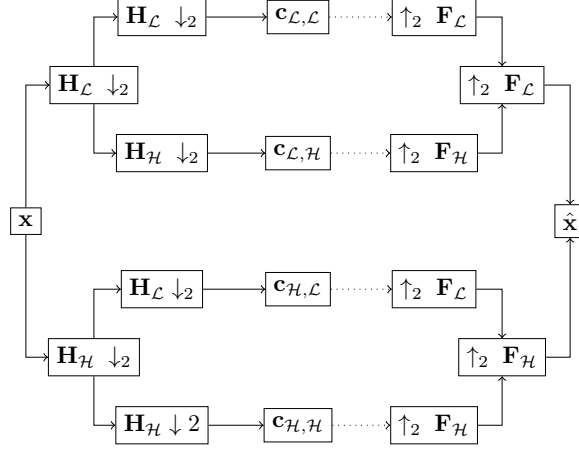


Figure 8: Schematic drawing of the full Wavelet Packet Transform ( $\mathcal{W}_p$ ) in a single dimension. Compared to Figure 7, the high-pass filtered side of the tree is expanded, too.

with  $k \in [\mathcal{L}, \mathcal{H}]$  and  $s \in \mathbb{N}_0$  the set of natural numbers, where  $\mathbf{x}_0$  is equal to the original input signal  $\mathbf{x}$ . At higher scales, the FWT uses the low-pass filtered result as input,  $\mathbf{x}_s = \mathbf{c}_{\mathcal{L},s}$  if  $s > 0$ . And  $*_1$  as the 1d-convolution operation. The dashed arrow in Figure 7 indicates that we could continue to expand the FWT tree here.

The Wavelet Packet Transform ( $\mathcal{W}_p$ ) additionally expands the high-frequency part of the tree. A comparison of Figures 7 and 8 illustrates this difference. Whole expansion is not the only possible way to construct a wavelet packet tree. See [19] for a discussion of other options. In both figures, capital letters denote convolution operators. These may be expressed as Toeplitz matrices [50]. The matrix nature of these operators explains the capital boldface notation. Coefficient subscripts record the path that leads to a particular coefficient.

We construct filter quadruples from the original filter pairs to process two-dimensional inputs. The process uses outer products [53]:

$$\mathbf{h}_a = \mathbf{h}_{\mathcal{L}}\mathbf{h}_{\mathcal{L}}^T, \mathbf{h}_h = \mathbf{h}_{\mathcal{L}}\mathbf{h}_{\mathcal{H}}^T, \mathbf{h}_v = \mathbf{h}_{\mathcal{H}}\mathbf{h}_{\mathcal{L}}^T, \mathbf{h}_d = \mathbf{h}_{\mathcal{H}}\mathbf{h}_{\mathcal{H}}^T \quad (8)$$

With  $a$  for approximation,  $h$  for horizontal,  $v$  for vertical, and  $d$  for diagonal [28]. We can construct a  $\mathcal{W}_p$ -tree for images with these two-dimensional filters. Figure 9 illustrates the computation of a full two-dimensional wavelet packet tree. More formally, the process initially evaluates

$$\mathbf{x}_0 * \mathbf{h}_j = \mathbf{c}_{j,1} \quad (9)$$

with  $\mathbf{x}_0$  equal to an input image  $\mathbf{X}$ ,  $j \in [a, h, v, d]$ , and  $*$  for two-dimensional convolution. At higher scales, all resulting coefficients from previous scales serve as inputs. The four filters are repeatedly convolved with all outputs to build the full tree. The inverse transforms work analogously. We refer to the standard literature [19, 50] for an extended discussion.

Compared to the FWT, the high-frequency half of the tree is subdivided into more bins, yielding a fine-grained view of the entire spectrum. We always show analysis and synthesis transforms to stress that all wavelet transforms are lossless. Synthesis transforms reconstruct the original input based on the results from the analysis transform.

### A.3 Histogram matching - InceptionV3

### A.4 Generative Architectures

Prior work mainly falls into the three GAN, Diffusion, and Variational AutoEncoder (VAE) architecture groups. The StyleGAN architecture family [22, 23, 21] is among the pioneering architectures in generative vision. GAN's allow rapid generation of high-quality images but suffer from training instability and poor mode coverage [43]. [45] proposes the Projected Fast GAN (Proj. FastGAN)-architecture, which stabilizes and improves training convergence by introducing ImageNet pre-trained weights into the discriminator. The upgraded discriminator pushes the output distribution towards

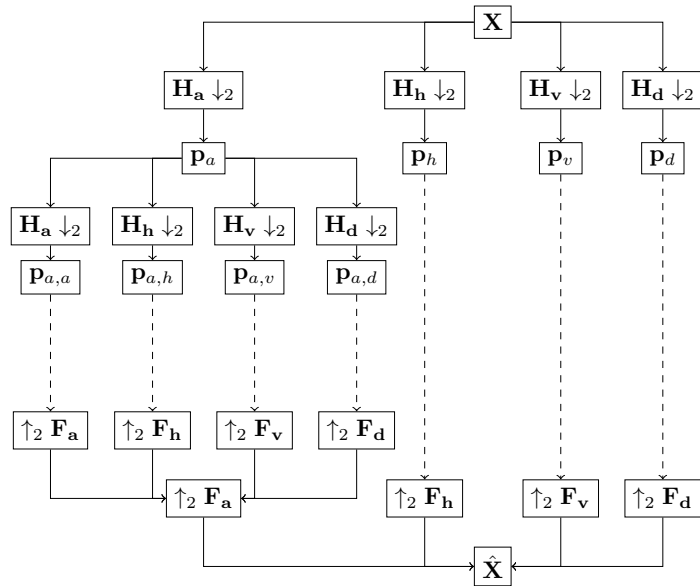


Figure 9: Two dimensional Wavelet Packet Transform ( $\mathcal{W}_p$ ) computation overview.  $\mathbf{X}$  and  $\hat{\mathbf{X}}$  denote input image and reconstruction respectively. We compute the Fréchet Wavelet Distance (FWD) using the wavelet packet coefficients  $\mathbf{p}$ . The transform is invertible, the distance computation is therefore based on a lossless representation.

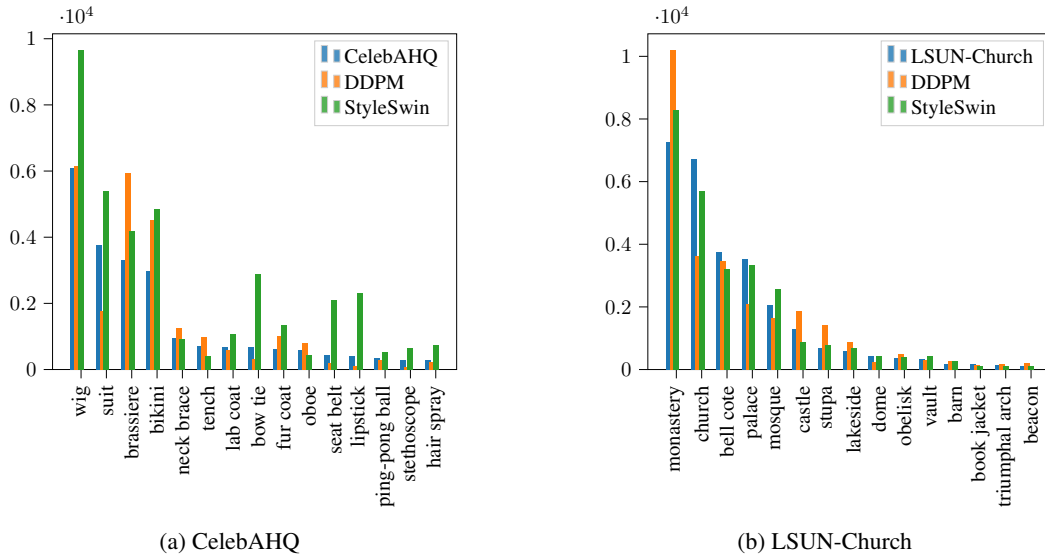


Figure 10: Histogram matching using top-15 classes from InceptionV3 network to explain the change in FID ranking changes between StyleSwin and DDPM on both (a) CelebAHQ and (b) LSUN church datasets.



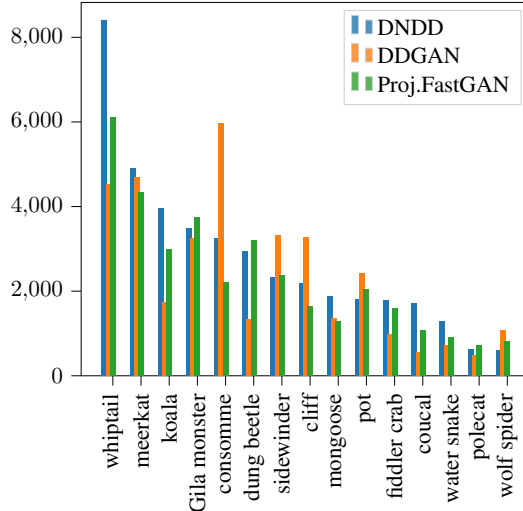


Figure 11: Top-15 classes from InceptionV3 network for DNDD-Dataset dataset, and images generated using Projected FastGAN and DDGAN. The distribution of top-15 classes for Proj. FastGAN matches with the dataset better than the DDGAN.

ImageNet. VAE models, on the other hand, [24, 51] enable the generation of diverse image sets, but are unable to produce high-quality images.

Diffusion models [48, 16, 38] have emerged as a very promising alternative and produce high-quality images [16, 7] in an autoregressive style. DDPMs, for example, are Markovian processes that learn to gradually separate added noise from data during training. During inference images are generated from Gaussian noise via a reverse process that requires iterating through all steps to generate an image. [49] reduced the number of sampling steps by introducing DDIM, which rely on a deterministic non-Markovian sampling process. Furthermore, [35] proposed the use of strided sampling, to reduce the sampling timesteps and also provide a performance improvement by using cosine- instead of linear sampling. Moreover, [35] adopt a weighted variational lower bound to supplement the Mean Squared Error (MSE) loss. In an attempt to solve the generative learning trilemma (image quality, diversity and fast sampling), [61] proposed Denoising Diffusion GAN (DDGAN). The paper parameterizes a conditional GAN for the reverse diffusion process and demonstrates faster generation speed.

## A.5 Compute details

In principle, our experiments run on single GPUs. For some experiments, we used up to 16 nodes with 4 Nvidia A40 GPUs each at a large scientific computing centre.

## A.6 DNDD-Dataset

DNDD-Dataset contains 3600 images with 7 classes. Networks are tasked with detecting nutrient deficiency in the soil, such as Sodium, Calcium, unfertilized, and 4 others. The images of sugar beet are captured over the 2019 growth period. Capturing occurred at the long-term fertilizer experiment (LTFE) Dikopshof near Bonn. The images were annotated with seven types of fertilizer treatments. The dataset is used for image classification and domain adaptation.

We train the Proj. FastGAN and DDGAN models on this dataset. We further preprocessed the dataset by splitting the 1000x1000 resolution image to 256x256 resolutions. This resulted in 57600 images overall. The training details are further provided in the main paper.